IOP Publishing | International Atomic Energy Agency Nuclear Fusion

Nucl. Fusion **61** (2021) 016029 (16pp) https://doi.org/10.1088/1741-4326/abc4c3

‘BAAE’ instabilities observed without fast ion drive

W.W. Heidbrink[1,*], **M.A. Van Zeeland**[2], **M.E. Austin**[3], **A. Bierwage**[4], **Liu Chen**[1,5], **G.J. Choi**[1], **P. Lauber**[6], **Z. Lin**[1], **G.R. McKee**[7] **and D.A. Spong**[8]

[1] University of California, Irvine, CA, United States of America
[2] General Atomics, San Diego, CA, United States of America
[3] University of Texas, Austin, TX, United States of America
[4] National Institutes for Quantum and Radiological Science and Technology, Rokkasho Fusion Institute, Aomori 039-3212, Japan
[5] Institute for Fusion Theory and Simulation and Department of Physics, Zhejiang University, Hangzhou, China
[6] Max Planck Institute for Plasma Physics, Boltzmannstr. 2, 85748 Garching, Germany
[7] University of Wisconsin, Madison, WI, United States of America
[8] Oak Ridge National Laboratory, Oak Ridge, TN, United States of America

E-mail: Bill.Heidbrink@uci.edu

Received 24 August 2020, revised 21 October 2020
Accepted for publication 26 October 2020
Published 10 December 2020

Abstract

The instability that was previously identified (Gorelenkov 2009 *Phys. Plasmas* **16** 056107) as a fast-ion driven beta-induced Alfvén-acoustic eigenmode (BAAE) in DIII-D was misidentified. In a dedicated experiment, low frequency modes (LFMs) with characteristic ‘Christmas light’ patterns of brief instability linked to the safety factor evolution occur in plasmas with electron temperature $T_e \gtrsim 2.1$ keV but modest beta. To isolate the importance of different driving gradients on these modes, the electron cyclotron heating (ECH) power and 80 keV, sub-Alfvénic neutral beams are altered for 50–100 ms durations in reproducible discharges. Although beta-induced Alfvén eigenmodes and reversed-shear Alfvén eigenmodes stabilize when beam injection ceases (as expected for a fast-ion driven instability), the LFMs that were called BAAEs persist. Data mining reveals that characteristic LFM instabilities can occur in discharges with no beam heating but strong ECH. A large database of over 1000 discharges shows that LFMs are only unstable in plasmas with hot electrons but modest overall beta. The experimental LFMs have low frequencies (comparable to diamagnetic drift frequencies) in the plasma frame, occur near the minimum of the safety factor $q_{\min}$, and appear when $q_{\min}$ is close to rational values. Theoretical analysis suggests that the LFMs are a low frequency reactive instability of predominately Alfvénic polarization.

Keywords: Alfven eigenmodes, fast ions, BAAE

(Some figures may appear in colour only in the online journal)

1. Introduction

In order to heat the fuel ions and minimize damage to vessel components, a tokamak reactor must confine fast ions. Low frequency modes (LFMs) that are driven unstable by the fast-ion population are of particular concern. At low frequency, the magnetic moment μ is conserved. If a fast ion resonates with a single wave of frequency ω and toroidal mode number n, the change in energy ΔW is related to the change in toroidal canonical angular momentum ΔP_ϕ by the relationship [1]

$$n\Delta W = \omega \Delta P_\phi. \tag{1}$$

---

[*] Author to whom any correspondence should be addressed.

Equation (1) implies that, for a given value of $n\Delta W$, the change in toroidal canonical angular momentum is largest for LFMs. Since P_ϕ depends on the poloidal flux, this implies that, for fast-ion driven modes where ΔW is appreciable, substantial spatial transport occurs. Therefore, LFMs that are driven by fast ions are dangerous. In contrast, small-amplitude non-resonant instabilities usually cause little fast-ion transport [2].

Theoretically, the beta-induced Alfvén-acoustic eigenmode (BAAE) is an eigenmode that sits in the gap created by coupling between the Alfvénic and acoustic continua [3–5]. The BAAE frequency is lower than the frequency of beta-induced Alfvén eigenmodes (BAE) [6] and reversed shear Alfvén eigenmodes (RSAE) [7]. Toroidal Alfvén eigenmodes (TAE) [8] have still higher frequencies. The BAAE polarization is mixed, while the polarizations of BAEs, RSAEs, and TAEs are primarily Alfvénic. Simulations with the ideal MHD code NOVA find a global eigenmode in the BAAE gap and a kinetic theory predicts their instability [3–5, 9]. Gyrokinetic codes have simulated modes that they identified as BAAEs [10–12]. Nevertheless, the nature of these modes remains controversial. The linear gyrokinetic code LIGKA found unstable modes in this frequency range that were cautiously dubbed 'low-frequency' modes [13], since their precise origin was uncertain. It was found [13–15] that regions of small damping appear close to the rational surfaces rather than in the MHD BAAE gap, and that the local frequencies scale with the diamagnetic frequency according to the kinetic dispersion relation. Subsequent gyrokinetic calculations with LIGKA show that simple analytical formulas for the BAE and BAAE frequency can be inaccurate [16]. Recent papers based on MHD calculations argue that there are many potentially unstable modes in the low frequency band, not just the BAE and the BAAE [17, 18]. Another complication is that, in the presence of strong toroidal rotation, MHD-theory predicts a flow-induced gap in the Alfvén spectrum [19, 20]. In kinetic treatments, the polarization of the continuum at low frequencies can vary rapidly [21, 22] and the coupling between modes is sensitive to the ratio of temperature and density gradients, as well as the ratio of the ion diamagnetic frequency to thermal transit frequency [21]. Theoretically, the mixed acoustic-Alfvénic polarization of the BAAE results in predictions of strong ion Landau damping [15, 23]. However, gyrokinetic GTC simulations of a tokamak with circular cross-section find [10–12] that BAAE excited by realistic fast ion density gradients have weak ion Landau damping because non-perturbative effects modify mode structures, resulting in a mostly Alfvénic polarization in the unstable BAAE, rather than the mixed acoustic-Alfvénic polarization of the damped BAAE that occurs in the absence of fast ion drive. Chen and Zonca [24] claim that energetic particles (EP) 'preferentially excite the BAE over the BAAE branch due to the stronger wave-EP interaction'. Clearly, improved understanding of the BAAE is needed to ascertain its importance in future devices.

Experimentally, unstable low-frequency modes that are distinguished from kinks, tearing modes, or fishbones have been observed on numerous devices. Instabilities that were identified as BAAEs were observed on magnetic diagnostics in low-density JET discharges with high electron temperature during hydrogen minority heating [3, 4]. In NSTX, modes identified as BAAEs were observed on magnetics in neutral-beam heated discharges [3–5]. In DIII-D, modes identified as BAAEs were observed in beam heated discharges by electron cyclotron emission (ECE) and density interferometer signals but were undetectable on magnetic diagnostics [5]. In all three of these cases, the publications state that the modes are driven by fast ions. In the case of DIII-D, data acquired by a fast-ion D-alpha (FIDA) diagnostic indicated degradation of fast-ion confinement in a period of the discharge when 'BAAEs' were the only observed instability [5], supporting the hypothesis that the modes were fast-ion driven instabilities. Modes identified as BAAEs were also observed during beam-heated discharges in HL-2A [25]. The magnitude and temporal evolution of the mode frequency agreed with analytical estimates of the BAAE frequency and, as in DIII-D, its appearance correlated with reduced neutron emission. 'Low-frequency' modes with frequencies below the BAE were observed by soft x-ray diagnostics in ASDEX-Upgrade discharges heated exclusively by ion cyclotron waves [13]. The modes occurred in the core close to the $q = 1$ surface near the beginning and end of the sawtooth cycle and had frequencies that increased with increasing electron temperature gradient ∇T_e. Modes resembling the DIII-D 'BAAEs' were also observed in ASDEX-Upgrade plasmas with intense electron cyclotron heating (ECH) (figure 3 of [26]). In EAST, frequency-sweeping modes that are labeled BAAE are observed by soft x-rays and ECE when the sawtooth cycle is relatively long in plasmas with combined ion-cyclotron, lower-hybrid, and neutral-beam heating [27].

Motivated by the need to better understand the stability of low-frequency fast-ion driven instabilities, in 2019 we conducted a dedicated experiment on DIII-D. As desired, discharges were created with two types of low-frequency modes that had been previously identified as BAEs and BAAEs. Analysis of the BAEs will appear in a separate paper; this paper focuses on the modes previously called BAAEs. As we will show, these modes are not really a BAAE. To avoid confusion, in this paper, the experimentally observed low-frequency mode that was previously identified as a BAAE is called a LFM.

The paper begins with the results of the dedicated experiment that showed that LFMs persist in the absence of beam injection (section 2). Following that surprising discovery, a search of archival DIII-D data revealed a set of low density discharges with strong ECH but no beam heating that also had LFM instabilities (section 3). The stability trends of the dedicated discharges and the ECH-only discharges are consistent with the parametric dependencies found in a much larger survey of over 1000 discharges (section 4). The experimental results are summarized in section 5. Theoretical analysis predicts a reactive instability with properties similar to the observations (section 6). Initial simulations are discussed next (section 7), followed by discussion and conclusion sections. Finally, an appendix reassesses the conclusions of an earlier paper [5] containing DIII-D LFM data.

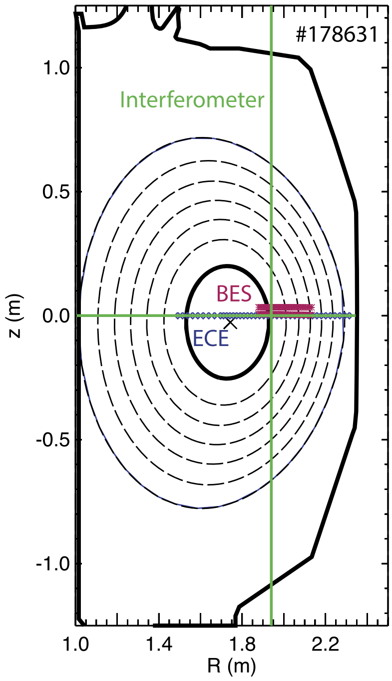

Figure 1. Elevation of DIII-D, showing flux surfaces (dashed lines), the $q_{\min}$ surface (thick line), the magnetic axis (X), and the locations of the instability diagnostics.

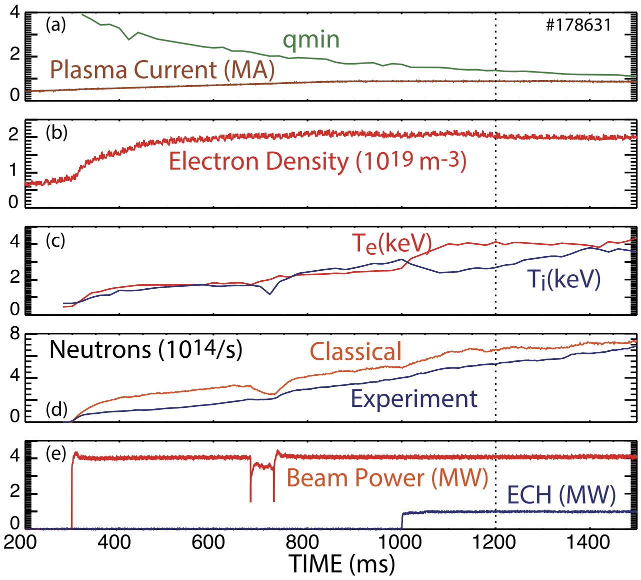

Figure 2. Time evolution of (a) plasma current I_{p} and $q_{\min}$, (b) line-averaged electron density $\bar{n}_{\mathrm{e}}$, (c) central electron temperature T_{e} and ion temperature T_{i}, (d) 'classical' and measured neutron rate, and (e) neutral beam and ECH heating power in the reference discharge of the dedicated experiment. The vertical dotted line indicates the time of interest.

2. Dedicated experiment

2.1. Plasma conditions and description of the instability

A dedicated experiment was conducted on DIII-D in 2019 to study the stability of BAEs and BAAEs. The plasma shape for these discharges is an elongated oval that is limited on the carbon inner wall (figure 1). The major radius is $R_0 = 1.74$ m, the horizontal minor radius is $a = 0.64$ m, and the toroidal field is 2.0 T. The fluctuations are measured by a 40-channel ECE radiometer [28], by the cross power of horizontal and vertical CO_2 interferometer chords [29], by a toroidal array of magnetic sensors at the outer midplane [30], and by beam emission spectroscopy (BES) [31]. For this experiment, the 64-channel BES diagnostic was configured as a 2×32 radial array from $R = 188$–213 cm separated vertically by 3.1 cm.

Figure 2 shows the time evolution of the reference discharge, #178631. The experiment is performed in the current ramp phase of an L-mode discharge. The q profile is obtained by EFIT equilibrium reconstructions [32] that utilize external magnetics and internal motional Stark effect (MSE) [33] data. These 'magnetics plus MSE' equilibrium reconstructions agree well with a reconstruction that includes kinetic pressure profile data and is further verified by the timing of the RSAEs (also known as 'Alfvén cascades' [7]) and by ECE data that show equal values of electron temperature on opposite sides of calculated flux surfaces. The q profile is reversed throughout the time of interest; sawteeth begin at 1724 ms. The electron density of the deuterium plasma is relatively low, $\bar{n}_{\mathrm{e}} \simeq 2 \times 10^{19}$ m^{-3}. All of the neutral beams employed in this experiment inject deuterium on the midplane in the co-current direction; the 'tangential' beams inject at a tangency radius of 115 cm, while the 'perpendicular' beams inject at $R_{\tan} = 76$ cm. With the exception of brief intervals, two tangential sources at 79 and 81 keV inject in the co-current direction throughout. From 1000–1500 ms, centrally deposited second harmonic 110 GHz ECH heats electrons. The electron temperature T_{e} increases during ECH, while the ion temperature T_{i} drops slightly. The expected 'classical' neutron rate in the absence of any transport by instabilities is calculated by the TRANSP NUBEAM code [34]. The measured neutron rate is lower than the classical prediction, indicating that one or more of the instabilities discussed below cause fast-ion transport.

Plasma profiles at the time of interest appear in figure 3. The electron density is measured by Thomson scattering [35] and profile reflectometry [36], T_{e} is measured by Thomson scattering and ECE, and the ion temperature, toroidal rotation, and carbon density are measured by charge exchange recombination spectroscopy of carbon impurities [37]. Carbon is assumed to make the dominant contribution to Z_{eff}.

Several different types of modes are unstable in these discharges (figure 4(b)). TAEs have relatively high frequencies that change gradually in time. The RSAEs are the modes above ~ 100 kHz with frequencies that increase rapidly in time. The BAEs have frequencies between ~ 100–150 kHz and are relatively wide in frequency. The LFMs are the briefly unstable modes between 20–100 kHz. They appear at regular intervals with ascending frequencies, resembling strings of Christmas lights. In this discharge, an ideal kink mode with frequency ~ 19.5 kHz and toroidal mode number $n = 3$ becomes unstable at 1220 ms. (The mode is identified as ideal because the phase is virtually constant as a function of radius.) All of the discharges in the dedicated experiment have similar RSAE, BAE, and LFM activity.

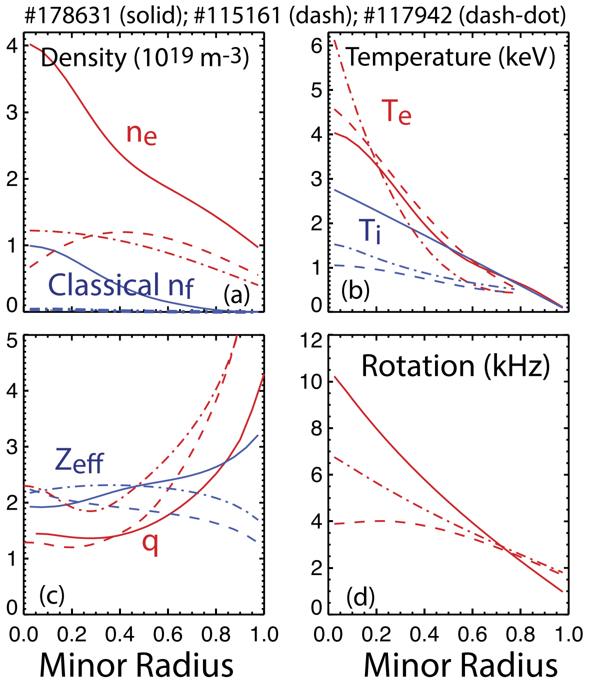

Figure 3. Profiles of (*a*) electron density and 'classical' fast-ion density calculated by TRANSP NUBEAM, (*b*) electron and ion temperature, (*c*) q and Z_{eff} and (*d*) toroidal rotation. The solid lines are the profiles at 1200 ms in the reference discharge of the dedicated experiment, the dash-dot lines are from the 'Christmas light' example of section 3 at 1200 ms, and the dashed line are from the 'mountain peaks' example of section 3 at 1600 ms. The abscissa is the normalized square root of the toroidal flux.

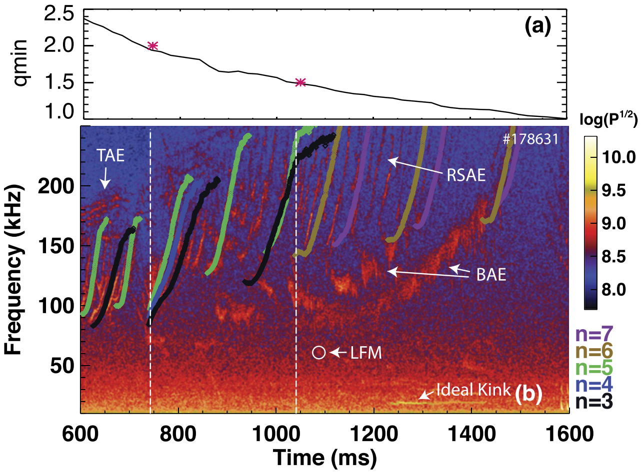

Figure 4. (*a*) Time evolution of $q_{\min}$ from EFIT reconstructions that utilize magnetics and MSE data. The asterisks show the times $q_{\min}$ crosses 2.0 and 1.5 as inferred from RSAE spectroscopy. (*b*) Cross-power of two interferometry chords. The expected evolution of RSAEs with various toroidal mode numbers are overlaid on the data. The vertical dashed lines mark the inferred times that $q_{\min}$ crosses 2.0 and 1.5. Examples of TAE, RSAE, BAE, LFM, and ideal kink activity are also labeled. (The barely visible LFM have a much larger signal-to-noise ratio on ECE signals than on the interferometer cross-power).

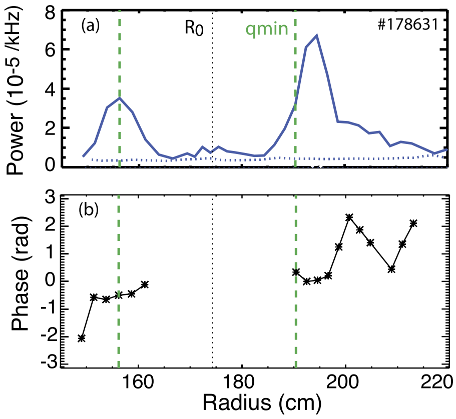

Figure 5. Radial (*a*) $\delta T_{\mathrm{e}}/T_{\mathrm{e}}$ cross-power and (*b*) cross-phase eigenfunction measured by ECE for the 48.8 kHz LFM at 1225 ms on the reference shot. The locations of the magnetic axis (dotted vertical line) and $q_{\min}$ surfaces (dashed vertical lines) are indicated. The noise floor (dotted line) is estimated from the median value of the spectrum within ±10 ms and ±10 kHz. For the phase, only measurements with statistically significant coherence are shown.

Figure 4(*a*) shows the good agreement between the values of $q_{\min}$ inferred from EFIT equilibrium reconstructions and the values of $q_{\min}$ inferred from the timing of RSAE activity.

The eigenfunctions of RSAE, BAE, and LFM instabilities are all localized near $q_{\min}$. Figure 5 shows the LFM eigenfunction measured by ECE for a typical mode in the reference shot. Peaks on both sides of the magnetic axis are usually evident. The normalized amplitude $\delta T_{\mathrm{e}}/T_{\mathrm{e}}$ is the same order of magnitude but slightly larger than the normalized amplitudes of RSAEs and BAEs in this discharge; the maximum amplitude of the mode in figure 5 is $\delta T_{\mathrm{e}} \simeq 25$ eV. In many cases, pairs of peaks separated by ~ 2 kHz are observed. Radial variations in phase similar to those illustrated in figure 5(*b*) are usually observed. In contrast, ideal modes, such as the one that appears from 1220–1410 ms in figure 4(*b*), maintain constant phase across the eigenfunction.

The LFMs are also often detected by BES. A complication for the BES data is that the injected beam that produces the measured beam emission contains fluctuations in the LFM band that sometimes obscures the mode activity, particularly for frequencies below 40 kHz. Radially, the detected modes are localized near $q_{\min}$, as for the ECE data.

In contrast to BAEs, LFMs are generally undetectable on the magnetics. As discussed below, the toroidal mode numbers of LFMs are typically higher than the $n = 2$ or $n = 3$ BAEs detected by magnetics, so their undetectably may be caused by weak coupling to magnetic probes at the wall, although weaker Alfvénic polarization of the LFMs might also play a role.

Although there are no direct measurements of the LFM toroidal mode number, both the poloidal mode number m and the toroidal mode number n can be confidently inferred from the q-evolution induced 'Christmas light' mode pattern. As shown in figure 4, the temporal evolution of $q_{\min}$ is known accurately. The toroidal rotation profile of carbon impurities and the radius of $q_{\min}$ are both known accurately, so the

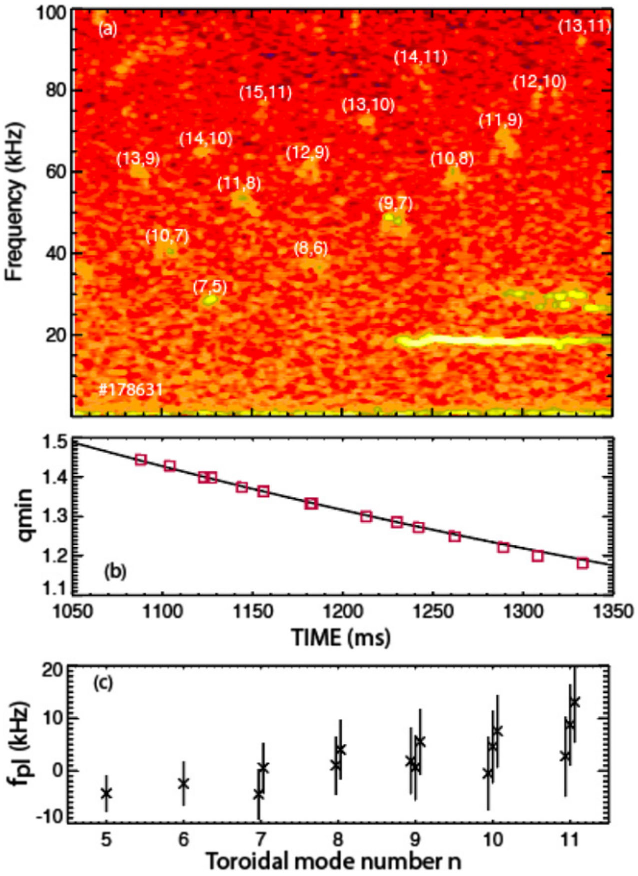

Figure 6. (*a*) ECE spectrum from channels near $q_{\min}$ on the reference discharge of the dedicated experiment, with each mode labeled by the (m, n) value that is consistent with the equilibrium. (*b*) $q_{\min}$ from the equilibrium reconstructions (line) and fitted rational q value m/n (symbols) vs time. (*c*) Inferred frequency in the plasma frame $f_{\mathrm{lab}} - nf_{\mathrm{rot}}$ vs fitted toroidal mode number. The error bars are based on an estimate of the uncertainty in f_{rot} at the location of $q_{\min}$.

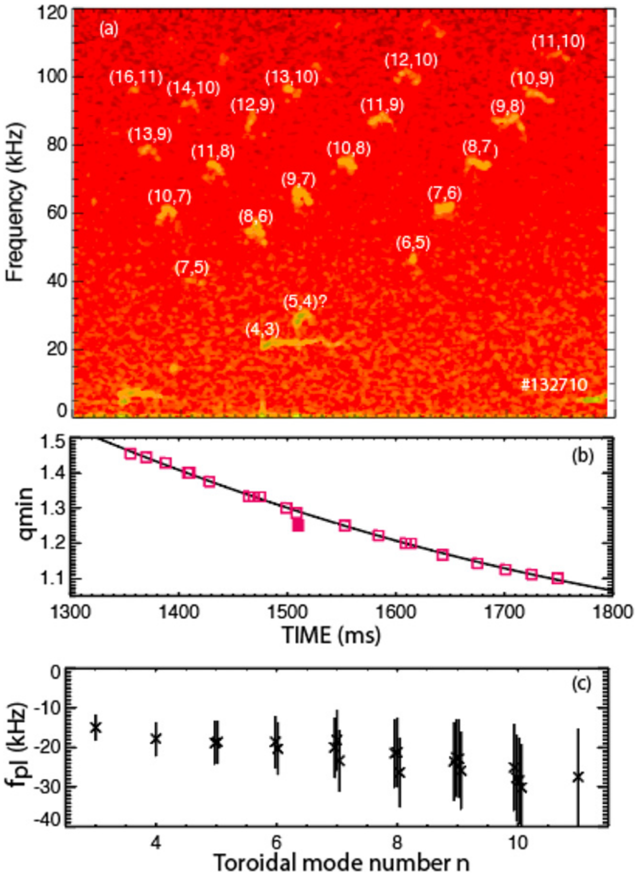

Figure 7. (*a*) ECE spectrum from channels near $q_{\min}$ on the same discharge as figure 5 of [5], with each mode labeled by the (m, n) value that is consistent with the equilibrium. (*b*) $q_{\min}$ from the equilibrium reconstructions (line) and fitted rational q value m/n (symbols) vs time. The solid point is the mode labeled '(5, 4)?' in the top panel. (*c*) Inferred frequency in the plasma frame $f_{\mathrm{lab}} - nf_{\mathrm{rot}}$ vs fitted toroidal mode number. The error bars are based on an estimate of the uncertainty in f_{rot} at the location of $q_{\min}$.

toroidal rotation at the mode location f_{rot} is also known accurately. Empirically, the frequency spacing between modes in the Christmas light pattern is close to f_{rot}. Assuming that (a) the unstable modes occur at rational values of $q_{\min}$ and (b) that different toroidal mode numbers have similar frequencies in the plasma frame, the observed temporal pattern of instability has a unique solution for its (m, n) values. Figure 6(*a*) shows this solution for the reference shot. Consider the 'string' of ascending modes that occurs between 1125–1350 ms. As one progresses up the string, both m and n increment by 1, and because the Doppler shift is nf_{rot}, the frequency increases by increments of f_{rot} as one progresses up the string. For this string, $m = n + 2$. For the ascending string between 1100–1250 ms, both m and n increment by 1 as one steps up the string but, for this string, $m = n + 3$. Similarly, an even earlier string has $m = n + 4$.

Figure 6(*b*) proves that this identification is correct. In this figure, the rational value of $q_{\min}$ at the time of appearance of each of the modes in the Christmas light pattern is compared with the measured value of $q_{\min}$ at that time. The agreement is excellent. For discharges like this where $q_{\min}(t)$ is known accurately and varies considerably, where f_{rot} is known, and the instability pattern consists of multiple ascending 'strings', the pattern of (m, n) values that fits the data is unique.

Unfortunately, poloidal mode structure measurements are unavailable for the dedicated experiment. However, for an earlier experiment [5], the BES diagnostic was configured to measure the poloidal phase near $q_{\min}$ on the low-field side of the torus. Figure 7(*a*) shows that this discharge has a Christmas light LFM pattern of instability that is similar to the pattern in the reference discharge of the dedicated experiment. As in the dedicated discharge, the assumption that the modes occur temporally at rational values of $q_{\min}$ with similar frequencies in the plasma frame yields a unique set of (m, n) assignments that are consistent with the measured $q_{\min}$ evolution (figure 7(*b*)). [There is one exception: the mode labeled '(5, 4)?' appears earlier than expected.] The availability of poloidal BES data in this discharge provides independent evidence that the interpretation of the spectrum is correct. Figure 8(*a*) shows the phase variation of an LFM for the five vertical columns shown in the inset. As expected, since the five columns are close in major radius, all five columns measure similar phase variation $\mathrm{d}\varphi/\mathrm{d}z$. The measured phase variation is related to the poloidal

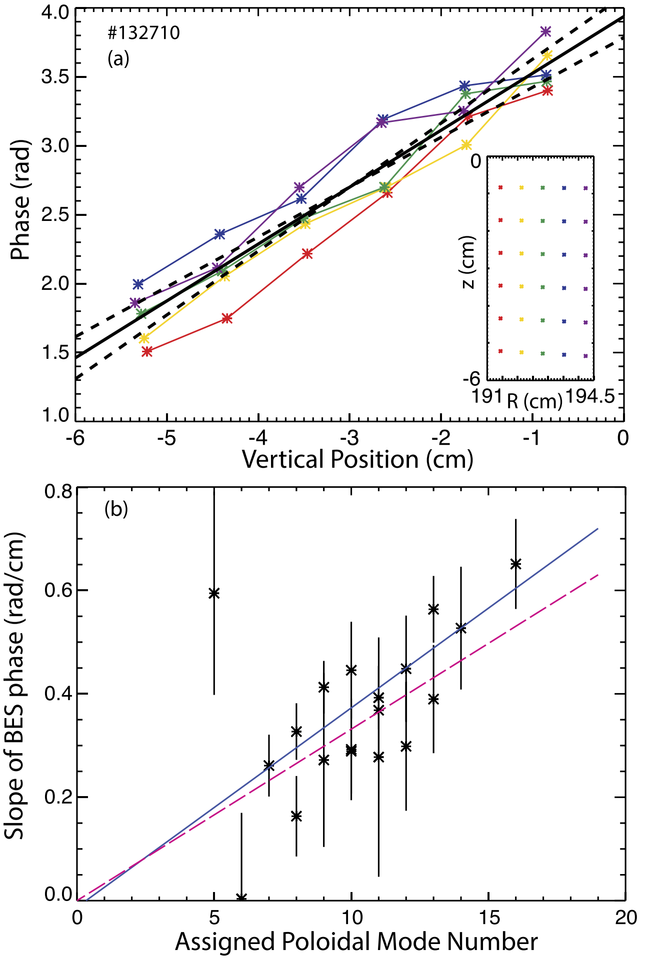

Figure 8. (*a*) Phase relative to an ECE reference signal vs vertical position for the 87 kHz LFM that appears at 1697 ms in the discharge of figure 7. The data are for the five color-coded vertical columns shown in the inset. The solid line is the weighted average of the slope; the dashed lines show ± one standard deviation. (*b*) $\mathrm{d}\varphi/\mathrm{d}z$ vs the poloidal mode number inferred from the Christmas light pattern for all of the modes shown in figure 7(*a*). The solid line is the weighted least-squares fit to the data and the dashed line is the prediction of equation (2).

wavenumber k_θ and mode number m by

$$\frac{\mathrm{d}\varphi}{\mathrm{d}z}=k_z\simeq k_\theta=\frac{gm}{r},\qquad(2)$$

where r is the minor radius at the position of the BES array. The parameter g is a geometrical factor that takes into account that the poloidal angle varies more slowly with position on the low-field side than on the high-field side; comparison of the poloidal angle in PEST coordinates [38] to a uniformly spaced geometrical poloidal angle gives $g = 0.75$ at the BES location in this case.

Figure 8(*b*) shows the measured value of $\mathrm{d}\varphi/\mathrm{d}z$ as a function of the assigned value of m for all of the LFMs in figure 7. Each plotted point and error bar is calculated as follows: the error in each individual measurement is inferred from the coherence with the reference signal, then the slope and its error are calculated from a weighted average of the individual measurements for each column, and finally the average slope and error are calculated from a weighted average of the values for the five columns. Figure 8(*b*) includes a weighted least-squares fit to these data. The fit passes very close to the origin; this would not occur if the assigned values of m were systematically shifted upwards or downwards. The figure also shows the slope predicted by equation (2). The good agreement between the prediction and the least-squares fit confirms that the assigned poloidal mode numbers are correct.

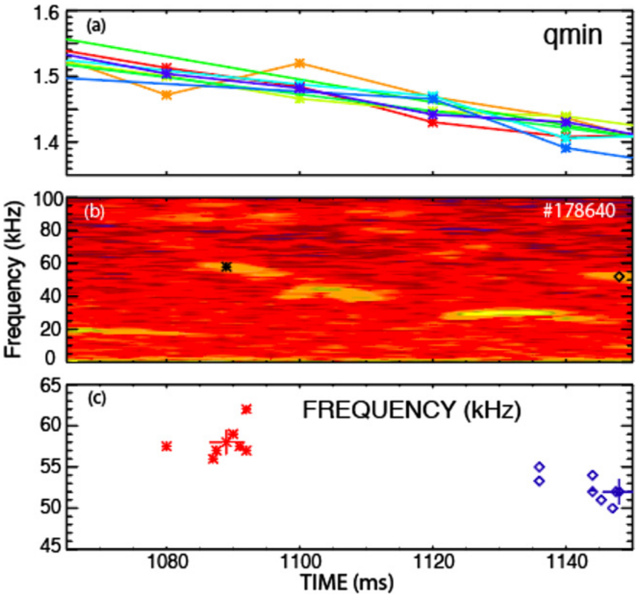

Figure 9. Reproducibility of q profile and mode evolution. (*a*) Evolution of q_{min} on eight nearly identical discharges prior to the time of interest. (*b*) Example from one discharge of two LFMs that appear in all eight discharges. (*c*) Frequency and time of appearance of the two modes in all eight discharges. The error bar shows the approximate uncertainty in determination of the frequency and time.

Figures 6(*c*) and 7(*c*) show the implied mode frequency in the plasma frame,

$$f_{\mathrm{pl}}=f_{\mathrm{lab}}-nf_{\mathrm{rot}},\qquad(3)$$

as a function of toroidal mode number. Here, a positive frequency indicates propagation in the ion diamagnetic direction, while a negative frequency indicates propagation in the electron direction. For six discharges where this analysis has been performed, the average value of f_{pl} is [3, −5, −8, −10, −21, −22] kHz. Evidently, the plasma-frame frequency is small, comparable to the rotation frequency. The uncertainty in f_{pl} is dominated by uncertainty in the toroidal rotation frequency; in addition to ∼ 10% uncertainty in the measurement itself, additional uncertainties are associated with determining the radial position of the eigenfunction (which, owing to radial shear in the rotation profile, alters f_{rot}), and possible differences between carbon and bulk-ion rotation. In the reference discharge, the calculated center of the BAAE gap using the analytical formula in [4] occurs at a frequency of ∼ 30 kHz. Although the actual mode frequency in the plasma frame is uncertain, it definitely is smaller than this calculated BAAE value.

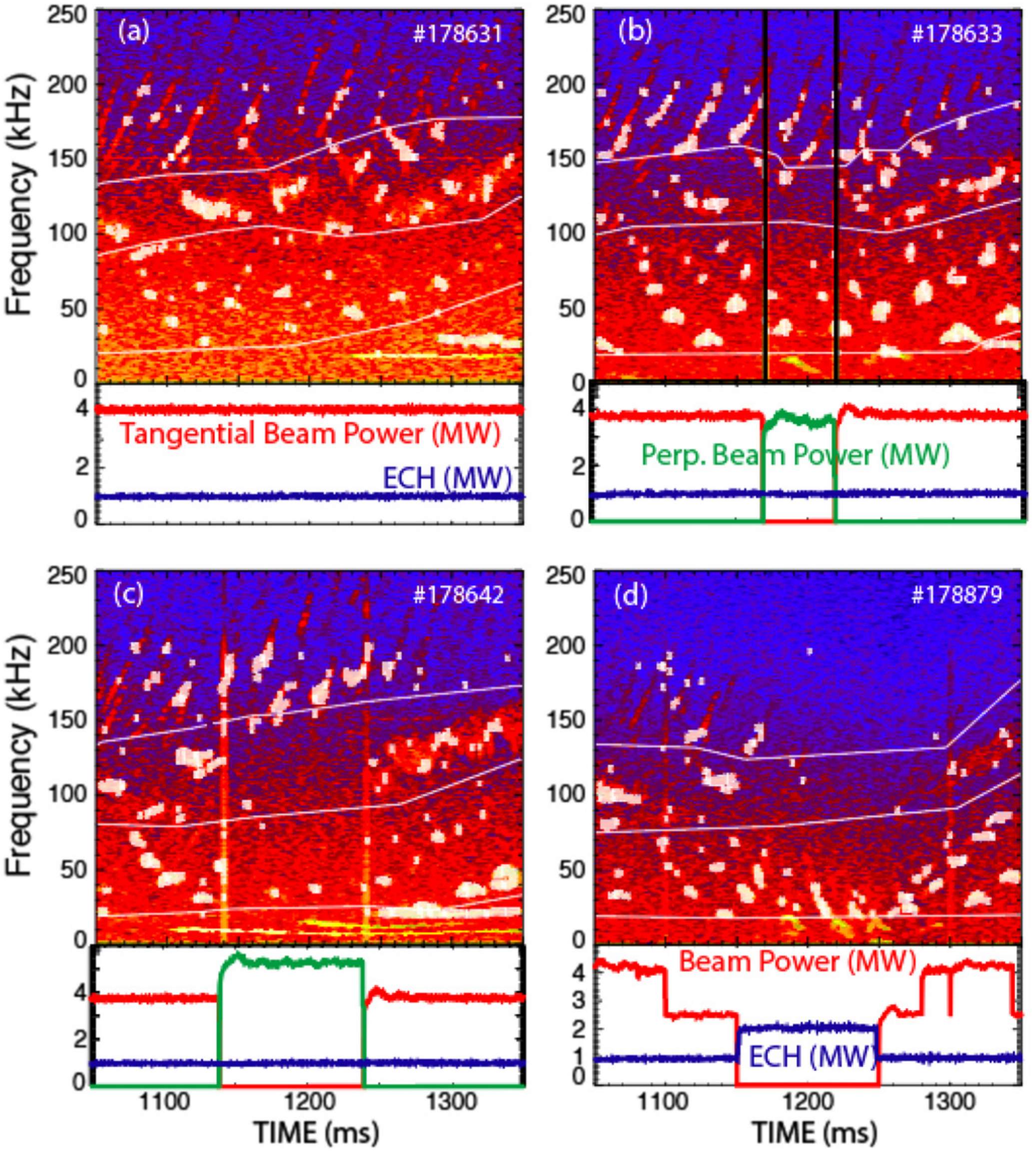

Figure 10. Time evolution of the ECE spectra, neutral beam power, and ECH power on four discharges. (*a*) Reference shot with steady injection of two tangential sources. (*b*) The two tangential sources are replaced by two perpendicular sources between 1170–1220 ms. (*c*) The two tangential sources are replaced by three perpendicular sources between 1140–1240 ms. (*d*) The beam power is turned off between 1150–1250 ms and the ECH power is increased. In all four panels, instabilities detected by the automatic peak finder are highlighted by white points; the white lines separate LFM, BAE, and RSAE frequency bands.

2.2. Stability properties

The primary goal of the dedicated experiment was to determine the relative importance of beam and thermal gradients in driving these low-frequency modes. To that end, the initial evolution of the discharges was held fixed so that the evolution of the q profile would be similar in every discharge. Figure 9 shows that this procedure was successful. The evolution of $q_{\min}$ as determined by 'MSE plus magnetics' equilibrium reconstructions is identical within random error on all eight discharges in figure 9(*a*). More importantly, the BAE and LFM activity are nearly identical. Figure 9(*c*) shows that LFMs with nearly identical frequencies appear at nearly the same time in all eight discharges. (Although not shown, this is also true for the BAEs.) Because the typical timescale for evolution of the q profile is on the order of seconds, this guarantees that changes in beam or ECH heating that last $\lesssim 100$ ms have little effect on the q profile evolution.

Figure 10 shows the principal results of the dedicated experiment. In the reference discharge (figure 10(*a*)) the heating is kept constant during the time of interest; consequently, the LFM and BAE activity continue unabated. In a pair of discharges, the two tangential beams are replaced by perpendicular beams that injected somewhat less (figure 10(*b*)) and somewhat more (figure 10(*c*)) power than in the reference discharge. In both discharges, the BAE activity was strongly affected by these changes. BAE activity between ~ 80–150 kHz quickly disappeared during perpendicular injection, then promptly reappeared when tangential injection resumed. Since the fast-ion slowing down time ($1/e$ energy loss time) is > 100 ms, this prompt response indicates that tangential ions near the injection energy are destabilizing these BAEs.

In contrast, LFM activity hardly changes when the beams switch from two tangential sources to two perpendicular sources (figure 10(*b*)). This indicates that high-energy tangential ions are *not* the principal destabilizing population for these modes. In the case with three perpendicular sources, the RSAE activity is stronger but the LFM activity becomes weak. High-energy perpendicular ions may be damping the LFMs but, as will be shown later, increased β is stabilizing for LFMs, so this is the most likely explanation for the reduction in LFM amplitude during the period with large perpendicular power.

Figure 10(*d*) shows a discharge where the beams are turned off entirely and the ECH power is increased to minimize changes to the background plasma. BAEs immediately disappear when the beams turn off and RSAEs disappear on a ~ 50 ms timescale; evidently, both of these modes are driven by the fast ions. In contrast, the LFMs drop in frequency but continue unabated. The primary reason for the reduction in LFM frequency is that the plasma rotation at q_{min} drops ~ 3 kHz between 1150 and 1250 ms, reducing the Doppler shift; a modest change of the LFM frequency in the plasma frame may also occur. This discharge clearly establishes that high-energy fast ions do *not* destabilize the LFMs.

The trends shown in figure 10 are consistently observed in all 20 discharges of the dedicated experiment. A database was compiled at 40 ms intervals between 1100–1300 ms for all 20 shots. In each interval, the mode activity was classified as ‘stable’, ‘marginal’, or ‘unstable’ in the LFM, BAE, and RSAE frequency bands. The boundaries between frequency bands are assigned by visual inspection (figure 10), guided by the analytical expressions for the RSAE, BAE, and BAAE frequencies found in the appendix of [39]. To quantify the mode activity, the ECE data are analyzed for coherent peaks. The raw ECE data is Fourier analyzed to calculate the cross-power between adjacent radial channels; this produces a large array of cross-power vs radius, time, and frequency. A coherent peak must satisfy the following four criteria.

(a) The power must be 2.0 times larger than the noise floor, where the noise floor is defined as the median cross-power within ±10 ms and ±10 kHz of the candidate peak.
(b) The peak must persist in time for at least 3 time bins. (Time bins separated by 2.4 ms are employed).
(c) The peak must persist in frequency for at least 3 frequency bins. (Frequency bins separated by 0.12 kHz are employed).
(d) The peak must appear in all three spatial channels near q_{min}.

Selected peaks are indicated by the white points in figure 10. (Note that constant noise peaks at, for example, 150 kHz are discarded.) To complete the database, kinetic profiles are fit for all 20 shots and the ‘classical’ fast-ion distribution function is analyzed by TRANSP NUBEAM [34].

Figure 11 shows the strongest dependencies in the database for LFMs. LFMs are observed when $T_{\text{e}} \gtrsim 2.2$ keV and when the poloidal beta $\beta_{\text{p}} \lesssim 0.5$. (Since the toroidal field, plasma current, and plasma shape are virtually identical for all of the dedicated shots, the β correlation is equally good with the toroidal beta β_{t} and normalized beta β_{N}.) Figure 11 also shows the trajectory of the discharge in figure 10(*d*) in this parameter space: when the beams turn off, β_{p} plummets but T_{e} remains high, so the LFMs remain unstable. The figure also shows the trajectory of a discharge similar to the one in figure 10(*c*): when perpendicular beams substitute for tangential beams, β_{p} remains elevated but T_{e} drops below 2.1 keV, causing the LFMs to stabilize.

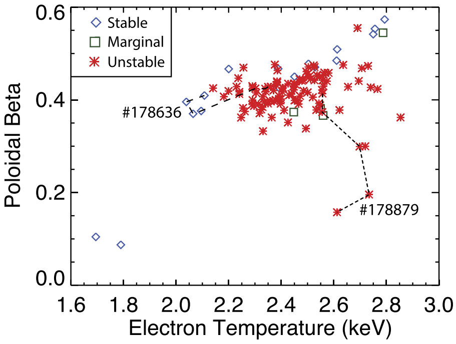

Figure 11. Dependence of LFM stability on electron temperature near q_{min} and on β_{p} for all of the discharges in the dedicated experiment. The dotted lines indicate the trajectory of the parameters in the discharge where the beams were turned off (#178879) and in a discharge where perpendicular beams substituted for tangential beams (#178636).

LFM stability does not depend directly upon beam power. Stable and unstable LFMs occur at all values of parallel beam beta $\beta_{b,\parallel}$ as calculated by TRANSP. The TRANSP calculation neglects instability-induced transport, so it is a measure of the potential instability drive. Quantitatively, the LFM power is essentially uncorrelated with $\beta_{b,\parallel}$ (correlation coefficient of $r = -0.14$). Similarly, the LFM power is uncorrelated with the perpendicular beam pressure, the neutron rate, and the product of beam power and slowing-down time $P_{\text{B}}\tau_{\text{s}}$. (The latter is a rough measure of the number of fast ions in the plasma.) Higher ion temperature gradients ∇T_{i} are anti-correlated with the LFM power, $r = -0.28$. This is in contrast to the BAEs, which correlate positively with beam beta, neutron rate, and $P_{\text{B}}\tau_{\text{s}}$.

3. LFMs in discharges without injected neutral beams

A search of archival DIII-D data reveals that modes with the ‘Christmas light’ LFM pattern are observed even in discharges with negligible beam heating. The discharges come from two different experiments, one that studied the correlation between rational values of q_{min} and the formation of internal transport barriers [40] and another that investigated the effect of particle transport on the current profile driven by electron cyclotron waves [41]. In both cases, early beam injection established a plasma with a reversed q profile in the first ~ 1.0 s of the discharge then, apart from rare beam pulses for diagnostic

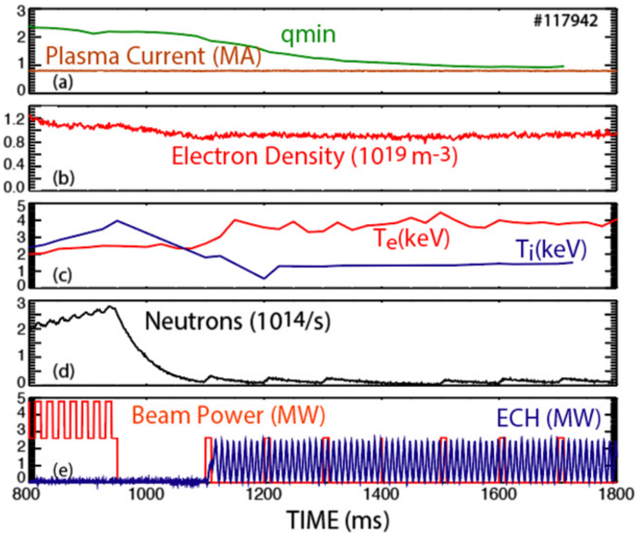

Figure 12. Time evolution of (*a*) plasma current I_p and q_min, (*b*) line-averaged electron density $\bar{n}_\mathrm{e}$, (*c*) central electron temperature T_e and ion temperature T_i, (*d*) measured neutron rate, and (*e*) neutral beam and ECH heating power in a discharge with the 'Christmas lights' instability pattern.

purposes, the beams were turned off prior to the onset of sawtooth activity during a period of intense ECH. Figure 12 shows a typical discharge. To accentuate the signal-to-noise on the ECE diagnostic and the particle transport effect, in both experiments, the plasma density was quite low, $\sim 1.0 \times 10^{19}$ m^{-3}. The resulting q profiles resemble q profiles during the time of interest in the dedicated experiment of section 2.

Figure 13(*a*) shows an example of a discharge with the Christmas light instability pattern in the ECE spectra. In this discharge, one diagnostic neutral beam that enables MSE and toroidal rotation measurements injected every 100 ms at 10% duty cycle. As figure 13(*a*) shows, the timing of the beam pulses has no effect on the instability pattern. Indeed, other discharges without any beams also exhibit the Christmas light pattern.

Plasma profiles for the discharge of figure 13 are overlaid on profiles from the dedicated experiment in figure 3. The electron density is low, the beam density is negligible, the electron temperature is large and strongly peaked, the ion temperature is low, and the q profile is weakly reversed. Since little torque is injected by the diagnostic beam pulses, the toroidal rotation is smaller than in the dedicated experiment. (It should be noted that, since the rotation measurement occurs during the beam pulse, between beam pulses, the rotation is expected to be smaller than the plotted value).

Just as in the dedicated experiment, the modes in this Christmas light pattern are correlated with the appearance of rational values of q. Comparison of figure 6(*a*) with figure 13(*a*) reveals a similar pattern of instability, with 'strings' of unstable modes with ascending values of n. Figure 13(*b*) shows that the agreement between the inferred values of m/n and the measured values of q_min is excellent. As in the dedicated experiment, the implied frequency in the plasma frame is low and possibly in the electron direction in this case (figure 13(*c*)).

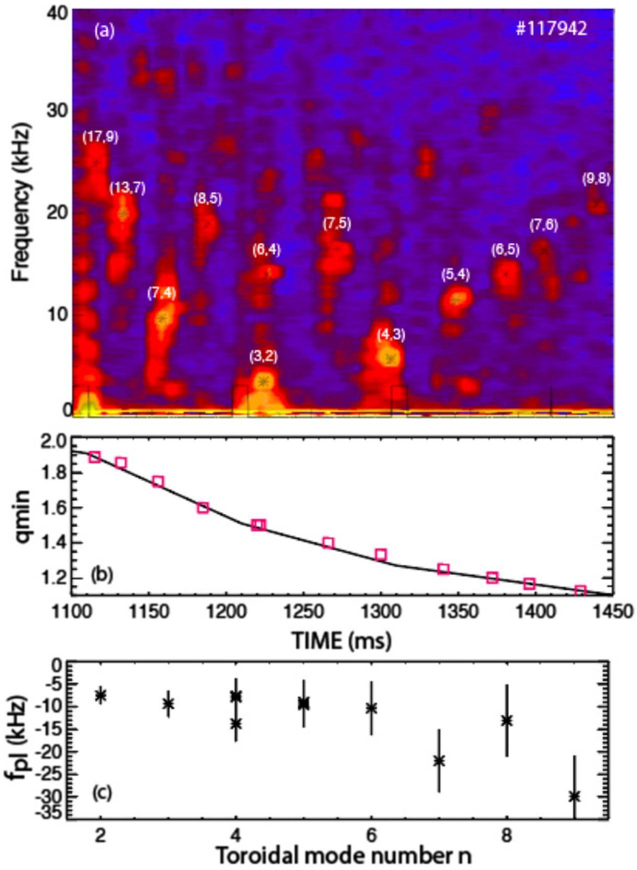

Figure 13. (*a*) ECE spectrum from channels near q_min on a discharge with a 'Christmas light' instability pattern, with each mode labeled by the (m, n) value that is consistent with the equilibrium. The timing of the diagnostic beam pulses are also shown. No modes are visible above 40 kHz. (*b*) q_min from the equilibrium reconstructions (line) and fitted rational q value m/n (symbols) vs time. (*c*) Inferred frequency in the plasma frame $f_\mathrm{lab} - nf_\mathrm{rot}$ vs fitted toroidal mode number. The error bars are based on an estimate of the uncertainty in f_rot at the location of q_min.

As in the dedicated experiment, the modes appear radially near q_min. In some discharges, ECE channels near the magnetic axis measure temperatures that are much larger than Thomson scattering, indicating the existence of a non-thermal electron population. This non-thermal population does not appear to affect the channels near q_min, which have temperatures consistent with Thomson scattering. The Christmas-light pattern (and the mountain-peaks pattern discussed below) occurs in discharges with and without a non-thermal electron population and the radial eigenfunction is similar either way.

Many discharges in these experiments manifest a different pattern of instability dubbed the 'mountain peaks' pattern. A typical example appears in figure 14(*a*). In these cases, each mode persists for longer than in the Christmas lights pattern, sweeping up and down in frequency over a ~ 20 ms time interval. A similarity to the Christmas lights pattern is that the maximum frequency grows successively larger by an amount comparable to the toroidal rotation frequency. Another similarity is that the timing of the peaks is determined by the evolution of the q profile, with the maximum frequency occurring at rational values of m/n (figure 14(*b*)). Another similarity

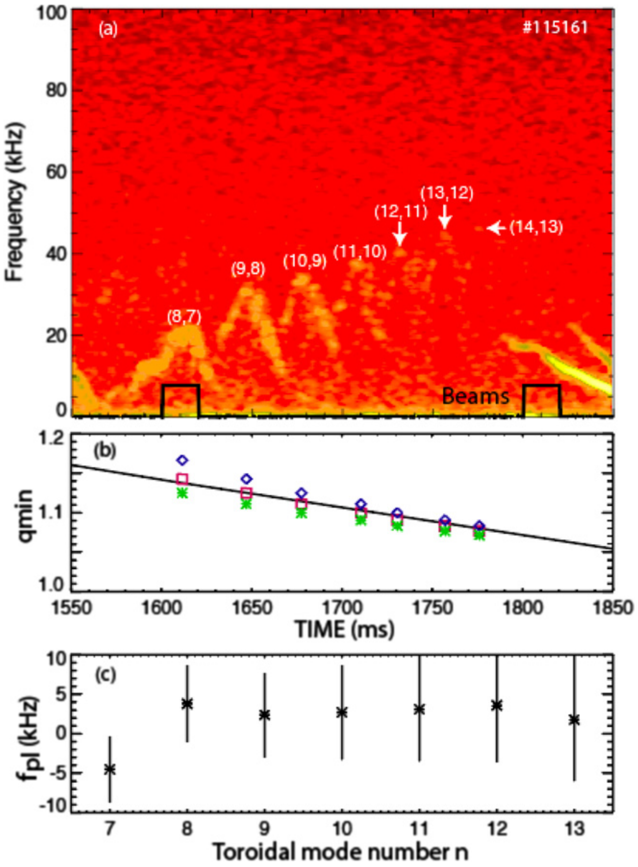

Figure 14. (*a*) ECE spectrum from channels near q_{min} on a discharge with a 'mountain peaks' instability pattern, with each mode labeled by the (m, n) value that is consistent with the equilibrium. The timing of the diagnostic beam pulses are also shown. (*b*) q_{min} from the equilibrium reconstructions (line) and fitted rational q value m/n (squares) vs time. The triangles (asterisks) show the evolution if the (m, n) assignments are incremented (decremented) by 1 (-1). (*c*) Inferred frequency in the plasma frame $f_{\mathrm{lab}} - nf_{\mathrm{rot}}$ vs fitted toroidal mode number. The error bars are based on an estimate of the uncertainty in f_{rot} at the location of q_{min}.

is that the inferred frequency in the plasma frame of the peak frequencies is quite low (figure 14(*c*)). A difference is that only a single 'strand' of ascending n numbers is readily apparent in any of the shots with the mountain peaks pattern.

For each 'mountain peak', the frequency sweeps over a range of 20 kHz or more in $\lesssim 10$ ms. Evidently, the mode frequency in the plasma frame must be non-zero over some of this range, as the plasma parameters hardly change on this timescale.

Another noteworthy feature of the mountain peaks pattern is illustrated by the mode at 1600 ms in figure 14(*a*). Note the 'kink' in the temporal evolution of the mode frequency when the diagnostic beam injects. This departure from the usual symmetrical mountain peak shape is caused by the change in the Doppler shift that occurs when the injected beam spins the plasma faster. It is also clear from this example that, for this mode, the amplitude of the instability is hardly affected by the fast ions injected midway through its appearance.

Plasma profiles for this case appear in figure 3. Generally speaking, the profiles are similar to the discharge with the Christmas lights pattern without beam injection. This particular discharge also has a hollow density profile associated with very strong central ECH and a flat T_{i} profile. Examination of all of the available data shows that the Christmas light pattern appears in relatively flat density profiles that may be slightly hollow, while the mountain peaks pattern appears both when the density profile is quite hollow and when it is nearly flat; also, the pattern occurs with T_{i} both flat and peaked.

As with the modes in the Christmas light pattern, the modes in the mountain peak pattern are localized near q_{min} and usually have appreciable phase variations in the radial eigenfunction.

Most likely, the two patterns are different manifestations of the same instability. Both are localized near q_{min}. Both occur in plasmas with similar q profiles, with q_{min} in the range of 1–2. Both typically appear for ~ 200 ms in the discharge. Both are undetectable on the magnetics. And, as discussed in the next section, both occur in the same plasma-parameter regime.

4. Large database

A large database has been assembled from 1112 DIII-D discharges acquired between 2008–2019. To ensure different values of q profile and to facilitate mode classification, selected times in the discharge are all during the first 1.9 s of the discharge, when the q profile steadily evolves. Selected experiments had a wide variety of purposes but nearly all dedicated energetic particle experiments are included. Time slices are chosen to sample either different plasma conditions or different types of mode activity, so a given discharge may have only a single entry or as many as nine entries. Selected conditions span plasma current $I_{\mathrm{p}} \leqslant 1.6$ MA, toroidal field $0.5 \leqslant B_{\mathrm{T}} \leqslant 2.1$, normalized beta $0.1 \leqslant \beta_{\mathrm{N}} \leqslant 3.2$, elongation $1.1 \leqslant \kappa \leqslant 2.2$, triangularity $-0.4 \leqslant \delta \leqslant 1.0$, line-average density $0.4 \times 10^{19} \leqslant \bar{n}_{\mathrm{e}} \leqslant 5.0 \times 10^{19}$ m^{-3}, central electron temperature $T_{\mathrm{e}} \leqslant 7.6$ keV, and central ion temperature $T_{\mathrm{i}} \leqslant 11.4$ keV. Plasmas in both L-mode and H-mode are included. All discharges utilize deuterium neutral beam injection into a deuterium plasma; carbon is the dominant impurity in the graphite-wall vessel.

Observed instabilities are classified as either EAE, TAE, RSAE, BAE, LFM, or EGAM. To classify the modes, ECE, interferometer, and magnetics cross-power spectra are typically examined. (If ECE is unavailable due to low field or high density, BES is examined instead.) Many discharges have steady low-frequency kinks or tearing modes with $n > 0$ that are not included in the database. Modes classified as an LFM have a Christmas light pattern similar to the ones in the dedicated experiment. To facilitate identification, the ECE data are subdivided into three different spatial regions and analytical formulas for the BAAE, BAE, RSAE, and TAE frequencies are overlaid on the spectra. (However, because the q profile is not always known accurately and RSAEs are readily recognized, when RSAEs are unstable, they are the primary guide to identification).

Modes are classified as 'stable' if they are unobservable, 'marginal' if they are barely observable and/or appear and

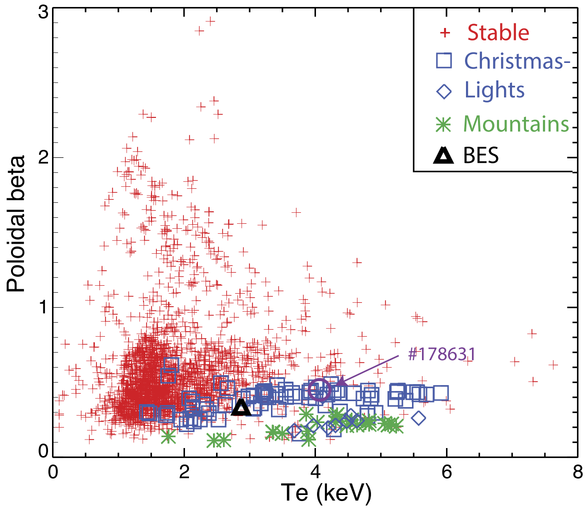

Figure 15. Occurrence of unstable 'Christmas light' LFMs vs central electron temperature and β_p in discharges with (square) and without (diamond) beam heating. No LFMs are observed on ECE, interferometer and magnetics spectra for 'stable' (+) conditions. Discharges with 'mountain peak' spectra$^{(*)}$ are also shown. The triangle represents the discharge of figure 16 that has detectable LFM-like modes on the BES but not on the ECE. The reference shot of the dedicated experiment is identified.

disappear, and 'unstable' if they are clearly visible like the modes in figure 4(*b*).

In addition to mode classification, the database includes all of the plasma shape, magnetic field, and beta information available from EFIT equilibrium reconstructions. Automated between-shots profile fitting provides kinetic temperature, rotation, and electron and impurity densities both at the plasma center and mid-radius, including their gradients. Neutral beam data include voltages, power, and directional information.

The resulting database reinforces the conclusions from the dedicated experiment of section 2. Figure 15 shows the counterpart of figure 11. As previously asserted, LFMs are most often observed in plasmas with relatively high electron temperature but relatively low β. Of the three measures of plasma beta, β_p provides a sharper stability boundary than β_N or β_T, probably because low toroidal field correlates with low T_e in the database. The electron temperature gradient ∇T_e correlates nearly as strongly with LFM stability properties as the central electron temperature but the correlation with electron pressure is weaker. For conditions with $1 < q_\mathrm{min} < 2$, instability requires $T_\mathrm{e}(0) > 1.4$ keV. One interpretation of figure 15 is that, despite substantial electron beta, LFMs require relatively low thermal and fast-ion beta in order to minimize ion Landau damping; however, the stability boundary correlates weakly with $T_\mathrm{e}/T_\mathrm{i}$, a key parameter in ion acoustic wave stability. The correlation of LFM stability is weak with all available neutral beam parameters.

Figure 15 also shows the discharges without beam heating (section 3) overlaid on the points from the large database. Like the beam-heated discharges, instability is observed when the electron temperature is high. The plasma beta is even lower than in the beam-heated discharges but this is likely an operational constraint, as neutral beams are the primary source of auxiliary heating at DIII-D.

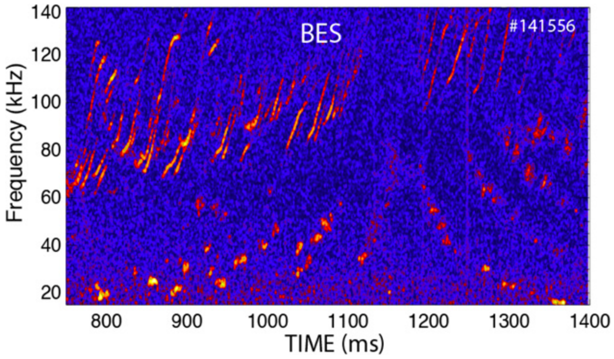

Figure 16. Cross-power spectra of several BES channels near q_min. The low-frequency modes are barely detectable on the ECE radiometer for this discharge.

Discharges with the mountain peaks pattern of instability occupy the same portion of parameter space as discharges with the Christmas light pattern (figure 15).

It should be noted that some conditions classified as stable may really have some unstable activity that could be detected by more careful examination of individual channels or other combinations of cross-power between diagnostics. In particular, on one pair of discharges that were heated exclusively by neutral beams, a Christmas-tree like pattern of unstable modes is readily discernible on the BES diagnostic (figure 16) but these same modes are at the noise level on the ECE diagnostic. These shots are classified as 'stable' in figure 15. Interestingly, the RSAE activity (the upsweeping modes above 60 kHz in figure 16) are clearly visible on both the BES and the ECE diagnostics in this discharge. Evidently, since both the RSAE activity and the low-frequency LFM activity occur near q_min, the weak LFM ECE signals are *not* caused by a reduction in ∇T_e in these discharges but must be associated with a change in the relative strength of the density $\tilde{n}_\mathrm{e}$ and temperature $\tilde{T}_\mathrm{e}$ fluctuations. As figure 15 shows, this discharge has similar values of T_e and β_p as other discharges with detectable LFM activity on the ECE. A second discharge with parameters similar to this one also has strong LFM activity on BES channels near q_min but a third discharge with more beam power and higher β_p does not, consistent with the general observation that large values of beta are stabilizing. The plasma parameters for this unstable discharge are rather similar to the profiles in the reference discharge of the dedicated experiment that are shown in figure 3.

In contrast, for the dedicated experiment, LFM modes are undetectable on both the BES and the ECE diagnostics for all discharges marked as 'stable' in figure 11.

Figure 17 uses a 'radar chart' to display the parametric dependence of the Christmas light LFM pattern. In this representation, the value of each variable is represented by a 'spoke' that extends from the origin and, for each database time slice, a line connects the different spokes. The figure shows that LFMs occur for relatively small values of T_i, β_p, and q_min but, for discharges with such small values of those parameters, T_e is relatively high. In contrast, the occurrence of LFMs depends

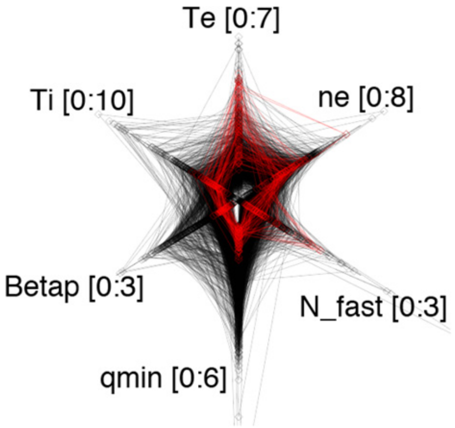

Figure 17. Radar chart of discharges with (red) and without (black) Christmas light LFM instabilities for the database of 1112 discharges. The six plotted variables are the central electron temperature in keV, the central ion temperature in keV, β_p, q_min, the number of fast ions in the plasma $P_\mathrm{B}\tau_\mathrm{s}$ in MW-s (where τ_s is the central $1/e$ energy slowing-down time), and the electron density in 10^{19} m^{-3}. The numbers in brackets are the lower and upper limits of the variable along that 'spoke'.

weakly on the electron density and on the number of fast ions in the plasma.

5. Summary of experimental results

The experimental findings can be divided into those that are virtually certain and those that are probable. Results known with high confidence for LFMs in DIII-D are the following. (The grounds for the conclusion appear in parenthesis).

(a) Large T_e or its gradient is essential for instability. (Figure 15).
(b) Fast ions are unimportant in destabilization. (Figure 10(*d*) and section 3).
(c) The mode occurrence is correlated with rational values of q. (The timing of the 'lights' in the pattern; examples appear in figures 6(*b*), 13(*b*) and 14(*b*)).
(d) Typical toroidal mode numbers are ∼ 3–12. (Figures 6, 13 and 14).
(e) The modes are localized near q_min. (ECE and BES data).
(f) Weak magnetic shear is destabilizing. (Timing of the Christmas light pattern in the discharge, as well as their localization near q_min).
(g) The mode frequency is low in the plasma frame, in the range of diamagnetic frequencies. (Figures 6(*c*), 13(*c*) and 14(*c*)).

The following findings are likely.

(h) Off-axis q_min is required. (This finding is based on the timing of the appearance of the Christmas light pattern relative to the first sawtooth, as well as EFIT equilibrium reconstructions. However, the accuracy of the equilibrium reconstruction in plasmas with weak shear is insufficient to *prove* that q_min is always off-axis).
(i) Thermal ions damp the mode. (As shown in figures 11 and 15, the Christmas light pattern occurs in discharges with high electron temperature but low beta. Since high T_e implies relatively strong electron pressure, the ion pressure must be relatively low in the unstable discharges).
(j) It is also possible that the modes have different polarization than typical shear Alfvén eigenmodes. (The modes are virtually always undetectable on magnetic diagnostics that measure vertical field fluctuations but RSAEs localized near q_min of comparable ECE amplitude also are normally undetectable for $n > 3$).

6. Theoretical analysis

To delineate the instability mechanisms, assume perturbations of a single high toroidal mode number, $n \gg 1$, that are localized about the reference mode-rational surface at $r = r_0$ where the magnetic shear, $s = r_0 q'/q$, is finite. In order that the discrete mode form a bound state, its effective inertial-layer parallel wave number, Λ, must asymptotically match the wave number in the ideal region; i.e., the following generalized fishbone-like dispersion relation (GFLDR) [23, 42, 43] applies:

$$i|s|\Lambda = \delta\hat{W}_f + \delta\hat{W}_{kt}. \tag{4}$$

Here, $\delta\hat{W}_f$ and $\delta\hat{W}_{kt}$ are normalized potential energies due to, respectively, the incompressible fluid and the magnetically trapped particles. The latter is approximately

$$\delta\hat{W}_{kt} \simeq 2\left(\frac{\pi q}{B}\right)^2 \sum_j m_j \int \mathrm{d}^3\mathbf{v}\left[\frac{\mathcal{E}^2(\hat{\omega}_* + \omega\partial/\partial\mathcal{E})F_0}{\bar{\omega}_d - \omega}\right]_j, \tag{5}$$

where $\mathcal{E} = v^2/2$, $\hat{\omega}_* F_0 = (\mathbf{k}\times\mathbf{b}/\omega_c)\cdot\nabla F_0$, $\bar{\omega}_d$ is the precessional frequency, and $j =$ species, including thermal and EP. Causality dictates that $\mathrm{Re}(\delta\hat{W}_f + \delta\hat{W}_{kt}) < 0$. Meanwhile, Λ satisfies the Alfvén-acoustic spectral relation,

$$\Lambda^2 = \Lambda_\mathrm{p}^2 + \Lambda_\mathrm{nc}^2, \tag{6}$$

where $\Lambda_\mathrm{p}^2 = \omega(\omega - \omega_{*\mathrm{pi}})/\omega_\mathrm{A}^2$ is the usual ion polarization term, $\omega_{*\mathrm{pi}}$ is the thermal ion diamagnetic drift frequency, the Alfvén frequency is $\omega_\mathrm{A} = v_\mathrm{A}/qR$, and Λ_nc^2 is the neoclassical enhancement term due to thermal-ion compression. Assuming that the mode frequency ω is lower than the thermal-ion bounce and transit frequencies, Λ_nc^2 is then given by [21, 44–46]

$$\Lambda_\mathrm{nc}^2 = c_0 \frac{q^2}{\sqrt{\epsilon}} \frac{(\omega - \langle\bar{\omega}_\mathrm{di}\rangle)(\omega - \omega_{*\mathrm{pi}})}{\omega_\mathrm{A}^2}, \tag{7}$$

where $\epsilon = r_0/R$, $\langle\bar{\omega}_\mathrm{di}\rangle$ is the average thermal-ion precession frequency, and $c_0 \simeq 1.6$ [47]. Note that $|\Lambda_\mathrm{nc}^2| \gg |\Lambda_\mathrm{p}^2|$. Equations (4), (6) and (7) then yield the following dispersion relation for the discrete low-frequency Alfvén modes (LFAM),

$$\frac{(\omega - \langle\bar{\omega}_\mathrm{di}\rangle)(\omega - \omega_{*\mathrm{pi}})}{\omega_\mathrm{A}^2} \simeq -\frac{\sqrt{\epsilon}}{q^2 c_0 s^2}\left(\delta\hat{W}_f + \delta\hat{W}_{kt}\right)^2. \tag{8}$$

Note that equation (8) indicates that instabilities can be either 'reactive' (non-resonant) or 'dissipative' (resonant) due to

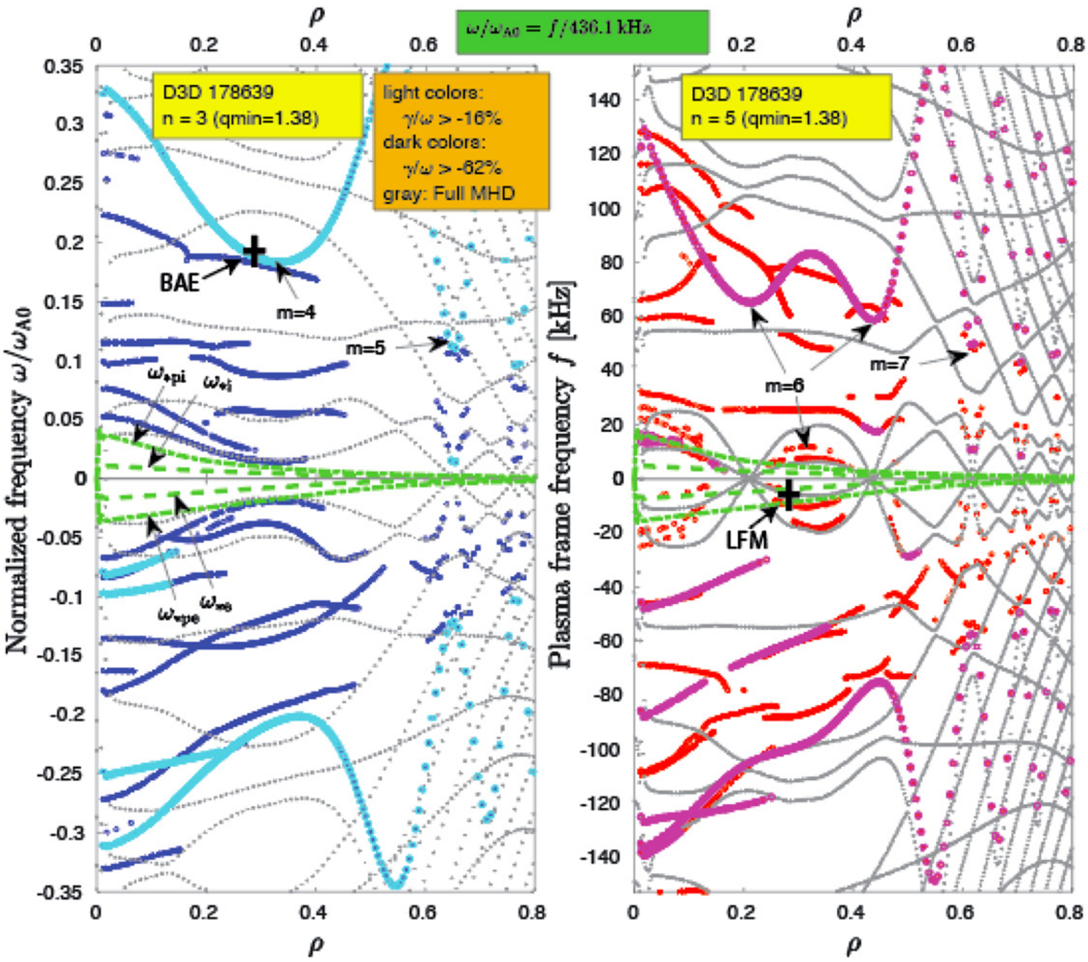

Figure 18. LIGKA calculation of (left) $n = 3$ and (right) $n = 5$ continua for the baseline case of the dedicated experiment at 1200 ms. Both diagrams show the same range of frequencies, with normalized units on the left and frequencies in kHz on the right. (Here, $\omega_{\mathrm{A}} = v_{\mathrm{A}0}/R_0$, where $v_{\mathrm{A}0}$ is the Alfvén speed at the magnetic axis.) The light colors indicate shear Alfvén wave branches and a few other continua with relatively low damping rates. Full MHD continua are shown in gray. The green lines represent ion and electron diamagnetic frequencies. The thick black cross on the left figure represents the experimental $n = 3$ BAE with a lab-frame frequency of 105.2 kHz at 1223 ms and the thick black cross on the right figure represents the experimental (6, 5) LFM with lab-frame frequency of 38 kHz observed at 1183 ms.

precessional resonance via $\mathrm{Im}(\delta\hat{W}_{kt})$. Focusing on the reactive instabilities where $\delta\hat{W}_{kt} \simeq \mathrm{Re}(\delta\hat{W}_{kt})$, the instability threshold is then given by

$$(2/qs)(\sqrt{\epsilon}/c_0)^{1/2}|\delta\hat{W}_f + \delta\hat{W}_{kt}| > |\omega_{*\mathrm{pi}} - \langle\bar{\omega}_{\mathrm{di}}\rangle|/\omega_{\mathrm{A}}. \quad (9)$$

Note that, for $T_{\mathrm{e}} \gg T_{\mathrm{i}}$, the dominant drive term on the left-hand side of the equation is due to thermal electrons; the energetic particle contribution is negligible since, for the EP, $|\omega_{*E}|$, $|\bar{\omega}_{dE}| \gg |\omega|$. On the other hand, the threshold condition on the right-hand side of the equation scales with T_{i} for a fixed toroidal mode number. In summary, this reactive LFAM instability has little coupling to EP, favors high T_{e} and low T_{i}, has $\omega_r \simeq \omega_{*\mathrm{pi}}/2$, and is essentially of Alfvénic polarization. It thus has little relation to the theoretical BAAE but does have properties consistent with the experimental LFM.

Although equation (9) successfully explains the parametric dependencies of the instability, the assumption of finite shear made in equation (4) is dubious at q_{min}; also, it is not obvious from equation (9) that the rapid frequency sweeping of the mountain peaks pattern (figure 14) is predicted. In fact, at rational surfaces where magnetic shear vanishes, the $i|s|\Lambda$ term on the lhs of equation (4) should be replaced by equation (3.18) of [43],

$$i|s|\Lambda \rightarrow iS(\Lambda^2 - k_{\|0}^2 L_0^2)^{1/2}$$
$$\times \left[(1/n)k_{\|0}L_0 - (i/n)(\Lambda^2 - k_{\|0}^2 L_0^2)^{1/2}\right]^{1/2}. \quad (10)$$

Here, $S = \left[r_0^2|q''|/q^2\right]^{1/2}$ and $|k_{\|0}L_0| = |nq_{\mathrm{min}} - m|$. When q_{min} sweeps through a rational value, $k_{\|0}$ rapidly changes and, presumably, causes a corresponding change in the real frequency. (Detailed confirmation of this expectation is left for future work).

7. Simulation

The kinetic theory presented in figure 3 of the original paper on BAAEs in DIII-D [5] predicted an unstable mode propagating at drift frequencies in the electron direction for DIII-D parameters.

Calculations were performed with the linear gyrokinetic code LIGKA [48] for the reference case of the dedicated experiment. In the absence of EPs, no discrete linear eigenmodes were found in LIGKA simulations, neither for the ion diamagnetic direction nor for the electron diamagnetic direction; in contrast, in the BAE band, LIGKA finds fast-ion driven modes. However, local analysis of the kinetic continua indicates regions of low thermal-ion Landau damping close to the (double) rational surfaces. (Note that the present version of LIGKA was not designed to analyze reactive modes with $\omega \simeq 0$.) The continua structure computed by LIGKA for adiabatic electrons and ions that are treated kinetically in the fast-passing limit (i.e., no kinetic contribution of trapped ions) is shown in figure 18. The figure shows that the frequency of the $(m, n) = (6, 5)$ mode observed near this time is low, comparable to diamagnetic frequencies and not related to any low-frequency continua or gaps.

The gyrofluid code FAR3d [49] finds unstable low-frequency modes with toroidal mode numbers similar to experiment for both the reference shot of the dedicated experiment (#178631) and for the 'mountain-peaks' example of figure 14, discharge #115161. As in the experiment, the growth rate of these modes is insensitive to the presence or absence of fast ions and the modes are localized near q_{min}. On the other hand, the growth rate and frequency do not depend strongly on the precise value of q_{min}, in contrast to the strong dependencies suggested by the Christmas light and mountain peaks patterns.

Detailed analysis of the reference discharge #178631 by the gyrokinetic code GTC will be reported elsewhere. In summary, global electromagnetic GTC simulations with gyrokinetic thermal ions find a linearly unstable low-frequency mode near q_{min} in the absence of fast ions. (With fast ions, the fastest growing eigenmode resembles the experimental BAE.) The unstable low-frequency modes have toroidal mode numbers $n = 3$–12 and frequencies in the plasma frame of 10–25 kHz, i.e., close to the ion diamagnetic frequencies and in the range observed experimentally. In agreement with the experimental dependence shown in figure 11, the linear growth rate increases rapidly with increasing electron temperature.

As expected, evaluation of the resonance condition in the reference discharge,

$$\omega = n\omega_{\phi} + p\omega_{\theta}, \tag{11}$$

shows that large numbers of recently-injected co-passing beam ions can resonate with modes with BAE frequencies but not with LFM frequencies. [Here, ω is the mode frequency, ω_{ϕ} is the toroidal precession frequency, ω_{θ} is the poloidal orbit frequency (all evaluated in the plasma frame), and p is an integer.] Figure 19 shows that the $p = 2$ resonance intersects the region of intense beam deposition for the experimental BAE but no resonances for the LFM intersect a heavily populated region.

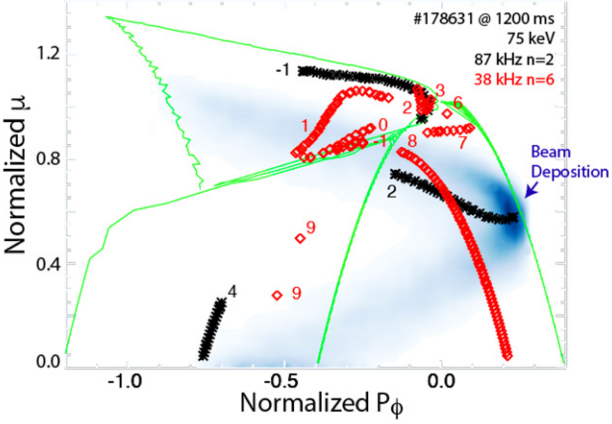

Figure 19. Resonances for 75 keV deuterium ions with the experimentally observed $n = 2$, 87 kHz BAE (X) and the $n = 6$, 38 kHz LFM (diamond) instabilities in the reference discharge of the dedicated experiment. Possible orbits are shown in constants-of-motion space using the canonical toroidal angular momentum $P_{\phi}/e\Psi_{\mathrm{LCFS}}$ and the magnetic moment $\mu B_0/E$, where Ψ_{LCFS} is the poloidal flux at the last closed flux surface, e is the elementary charge, and B_0 is the magnetic field at the magnetic axis. The green lines indicate topological boundaries and the blue shading shows where fast ions are deposited by the tangential beams. (The beam deposition is greatest for co-passing ions near the magnetic axis.) The numbers beside the symbols are the values of p that satisfy the resonance condition in equation (11). In addition to satisfying equation (11), the plotted resonant orbits traverse the region near q_{min}.

8. Discussion

Although other experiments have observed instabilities that they called BAAEs, only DIII-D and ASDEX-Upgrade [26] have reported the Christmas light pattern of instability; however, this difference could be because the temporal evolution of the q profile was different. The modes observed on JET [3, 4] have much in common with the DIII-D modes: the electron temperature is relatively high, there is no beam injection so the ion beta is relatively low, the mode frequency is low, and the modes occur prior to the onset of sawteeth. Perhaps the longer duration of the modes occurs because the q profile evolves more slowly in the hotter, larger, JET plasma. This may also explain differences with the ASDEX-Upgrade results reported in [13]. Their modes were observed in discharges with ion cyclotron heating exclusively, i.e., in plasmas with relatively low ion beta. The modes occurred at distinct times in the sawtooth cycle, perhaps when q_{min} was off-axis and had weak shear. Interestingly, the mode frequencies increased and decreased with changes in ∇T_{e}. Similarly, at EAST [27], the low-frequency modes called BAAEs only occur during discrete periods in the sawtooth cycle and they occur in plasmas with combinations of auxiliary heating that make off-axis q_{min} profiles probable.

In contrast, it seems that the NSTX modes [3–5] are likely a different instability, as they occur in beam-heated plasmas during the current ramp but have a different temporal evolution and are readily detected by the magnetics. The mode identified as a BAAE on HL-2A

[25] also appears to be a different instability than the DIII-D LFM.

Unstable modes in plasmas with strong electron heating but no beam heating have been observed in other tokamaks. For example, modes with frequencies in the TAE band were observed in COMPASS-D [50]. Fishbones driven by electrons have been observed in numerous devices, including [51].

9. Conclusion

Contrary to expectation, the instability that was previously identified as a fast-ion driven BAAE in DIII-D is *not* driven by fast ions. Rather, the instability depends most strongly on electron parameters. The frequency of the mode in the plasma frame is comparable to diamagnetic drift frequencies and is lower than the center of the BAAE gap. Theoretical analysis suggests that it is a reactive instability, probably a low frequency Alfvén mode. Measurements of the mode polarization are needed to confirm this identification. The experimental results are consistent with Chen and Zonca's qualitative prediction [24] that EP 'preferentially excite the BAE over the BAAE branch due to the stronger wave-EP interaction'.

Because the instability does not appear to resonate with fast ions, it is unlikely to cause appreciable fast-ion transport. Because of their large orbits, EP usually phase-average over non-resonant perturbations of modest amplitude and limited spatial extent, reducing their transport relative to thermal particles [2]. If the isotropic alpha-particle population in future devices behaves like anisotropic beam ions in DIII-D, then resonant low frequency instabilities such as the BAE are of greater concern, but detailed calculations are needed to determine if this is the case. The implications for future devices of the BAE and LFM data acquired in the dedicated experiment will be the subject of a forthcoming paper. Detailed simulations of these plasmas by GTC will also be published elsewhere.

Acknowledgments

Helpful discussions with Xiaodi Du, Nate Ferraro, Nikolai Gorelenkov, Craig Petty, and Fulvio Zonca are gratefully acknowledged, as is the vital assistance of the DIII-D team. This work is supported by US Department of Energy award DE-SC0020337 and DE-FC02-04ER54698. This report was prepared as an account of work sponsored by an agency of the United States Government. Neither the United States Government nor any agency thereof, nor any of their employees, makes any warranty, express or implied, or assumes any legal liability or responsibility for the accuracy, completeness, or usefulness of any information, apparatus, product, or process disclosed, or represents that its use would not infringe privately owned rights. Reference herein to any specific commercial product, process, or service by trade name, trademark, manufacturer, or otherwise, does not necessarily constitute or imply its endorsement, recommendation, or favoring by the United States Government or any agency thereof. The views and opinions of authors expressed herein do not necessarily state or reflect those of the United States Government or any agency thereof. This work has been partially carried out within the framework of the EUROfusion Consortium and has received funding from the Euratom research and training program 2014–2018 and 2019–2020 under Grant agreement No. 633053. The views and opinions expressed herein do not necessarily reflect those of the European Commission.

Appendix. Reassessment of previously published DIII-D data

The new data and analysis have spurred reexamination of the DIII-D results that were previously published. In [5], the modes shown in figure 7 were found to have frequencies in the plasma frame consistent with BAAEs while, in the present work, the inferred frequencies are too low to be BAAEs. The source of this discrepancy is the different values of toroidal mode number n assigned to the modes. In the absence of direct measurements, Gorelenkov *et al* [5] used toroidal mode numbers from the MHD code NOVA. The modes found by NOVA appear temporally after the rational $q_{\min} = m/n$ crossing and after the continuum tip has reached the BAAE gap, possibly later than in the experiment; see figure 5(*b*) of [5]. These toroidal mode numbers are smaller than the ones found by fitting the entire Christmas light pattern (figure 7). As a result, in the earlier work, the Doppler shift correction nf_{rot} (equation (3)) is smaller and the inferred frequency in the plasma frame is higher. However, the mode numbers assigned by NOVA cannot be made to fit the temporal evolution of $q_{\min}$ for all of the modes in the pattern; also, the BES data require higher values of m (figure 8). The true value of toroidal mode number is higher than previously assumed, so the frequency in the plasma frame is lower than the calculated center of the BAAE gap (39 kHz in this discharge).

Section IV of [5] asserts that the BAAEs are responsible for enhanced fast-ion transport. This conclusion was based on the observation that, in a time when exclusively LFM activity was visible on the available diagnostics, the neutron and FIDA signals were lower than predicted by 'classical' TRANSP NUBEAM calculations that assume negligible instability-induced transport. Reexamination of the data confirms that only Christmas-light LFMs are apparent in interferometer and ECE data. Reanalysis of the fast-ion data during this period shows that the neutron rate is $\sim 92\%$ of the classical prediction, while the central FIDA data are $\sim 2/3$ of the classical expectation. (Because the neutron measurement is volume-averaged but the FIDA measurement is local, the FIDA deficit usually exceeds the neutron deficit.) Although this deficit is smaller than previously reported, it does appear that the previous assertion of degraded fast-ion confinement was valid. Perhaps this old discharge had undetected AEs at higher frequency that degraded fast-ion confinement. Or perhaps LFMs degrade fast-ion confinement without extracting sufficient energy to appreciably alter mode stability. Unfortunately, in the discharges of the dedicated experiment reported here, either multiple instabilities were unstable or the beams needed for fast-ion transport measurements were turned off, so it is not possible to determine the effect of LFMs on fast-ion transport unambiguously for the recent data.

ORCID iDs

W.W. Heidbrink https://orcid.org/0000-0002-6942-8043
M.A. Van Zeeland https://orcid.org/0000-0002-7911-2739
A. Bierwage https://orcid.org/0000-0003-1243-0502
G.J. Choi https://orcid.org/0000-0003-0044-1650
D.A. Spong https://orcid.org/0000-0003-2370-1873

References

[1] Chen L., Vaclavik J. and Hammett G.W. 1988 *Nucl. Fusion* **28** 389
[2] Heidbrink W.W. and White R.B. 2020 *Phys. Plasmas* **27** 030901
[3] Gorelenkov N.N., Berk H.L., Fredrickson E. and Sharapov S.E. 2007 *Phys. Lett.* A **370** 70
[4] Gorelenkov N.N. *et al* 2007 *Plasma Phys. Control. Fusion* **49** B371
[5] Gorelenkov N.N. *et al* 2009 *Phys. Plasmas* **16** 056107
[6] Heidbrink W.W., Strait E.J., Chu M.S. and Turnbull A.D. 1993 *Phys. Rev. Lett.* **71** 855
[7] Sharapov S.E., Testa D., Alper B., Borba D.N., Fasoli A., Hawkes N.C., Heeter R.F., Mantsinen M. and Von Hellermann M.G. 2001 *Phys. Lett.* A **289** 127
[8] Cheng C.Z., Chen L. and Chance M.S. 1985 *Ann. Phys.* **161** 21
[9] Eremin D.Y. and Könies A. 2010 *Phys. Plasmas* **17** 012108
[10] Liu Y., Lin Z., Zhang H. and Zhang W. 2017 *Nucl. Fusion* **57** 114001
[11] Zhang H.S., Liu Y.Q., Lin Z. and Zhang W.L. 2016 *Phys. Plasmas* **23** 042510
[12] Cheng J. *et al* 2017 *Phys. Plasmas* **24** 092516
[13] Curran D., Lauber P., Carthy P.J.M., da Graca S. and Igochine V. 2012 *Plasma Phys. Control. Fusion* **54** 055001
[14] Zonca F., Chen L. and Santoro R.A. 1996 *Plasma Phys. Control. Fusion* **38** 2011
[15] Lauber P. 2013 *Phys. Rep.* **533** 33
[16] Bierwage A. and Lauber P. 2017 *Nucl. Fusion* **57** 116063
[17] Cheng C.Z., Kramer G.J., Podesta M. and Nazikian R. 2019 *Phys. Plasmas* **26** 082508
[18] Kramer G.J. *et al* 2020 *Plasma Phys. Control. Fusion* **62** 075012
[19] Van Der Holst B., Belien A.J.C. and Goedbloed J.P. 2000 *Phys. Rev. Lett.* **84** 2865
[20] Van Der Holst B., Belien A.J.C. and Goedbloed J.P. 2000 *Phys. Plasmas* **7** 4208
[21] Chavdarovski I. and Zonca F. 2004 *Phys. Plasmas* **21** 052506
[22] Falessi M.V., Carlevaro N. and Fusco V. 2020 *J. Plasma Phys.* **86** 845860501
[23] Zonca F. and Chen L. 2014 *Phys. Plasmas* **21** 072121
[24] Chen L. and Zonca F. 2017 *Phys. Plasmas* **24** 072511
[25] Liu Y. *et al* 2012 *Nucl. Fusion* **52** 074008
[26] Sharapov S.E. *et al* 2018 *Plasma Phys. Control. Fusion* **60** 014026
[27] Xu M. *et al* 2020 *Nucl. Fusion* **60** 014026
[28] Austin M.E. and Lohr J. 2003 *Rev. Sci. Instrum.* **74** 1457
[29] Zeeland M.A.V., Kramer G.J., Nazikian R., Berk H.L., Carlstrom T.N. and Solomon W.M. 2005 *Plasma Phys. Control. Fusion* **47** L31
[30] Strait E.J. 2006 *Rev. Sci. Instrum.* **77** 023502
[31] Gupta D.K., Fonck R.J., Mckee G.R., Schlossberg D.J. and Shafer M.W. 2004 *Rev. Sci. Instrum.* **75** 3493
[32] Lao L.L., St. John H., Stambaugh R.D., Kellman A.G. and Pfeiffer W. 1985 *Nucl. Fusion* **25** 1611
[33] Rice B.W., Nilson D.G. and Wróblewski D. 1995 *Rev. Sci. Instrum.* **66** 373
[34] Pankin A., Mccune D., Andre R., Bateman G. and Kritz A. 2004 *Comput. Phys. Commun.* **159** 157
[35] Carlstrom T.N. *et al* 1992 *Rev. Sci. Instrum.* **63** 4901
[36] Wang G. *et al* 2006 *Nucl. Fusion* **46** S708
[37] Gohil P., Burrell K.H., Groebner R.J. and Seraydarian R.P. 1990 *Rev. Sci. Instrum.* **61** 2949
[38] Grimm R.C., Dewar R.L. and Manickam J. 1983 *J. Comput. Phys.* **49** 94
[39] Van Zeeland M.A. *et al* 2019 *Nucl. Fusion* **59** 086028
[40] Austin M.E. *et al* 2006 *Phys. Plasmas* **13** 082502
[41] Petty C.C., Austin M.E., Lohr J., Luce T.C., Makowski M.A., Prater R., Harvey R.W. and Smirnov A.P. 2010 *Fusion Sci. Technol.* **57** 10
[42] Zonca F. and Chen L. 2014 *Phys. Plasmas* **21** 072120
[43] Chen L. and Zonca F. 2016 *Rev. Mod. Phys.* **88** 015008
[44] Zonca F. *et al* 2007 *Nucl. Fusion* **47** 1588
[45] Chavdarovski I. and Zonca F. 2009 *Plasma Phys. Control. Fusion* **51** 115001
[46] Li Y.Y. 2020 private communication.
[47] Rosenbluth M.N. and Hinton F.L. 1998 *Phys. Rev. Lett.* **80** 724
[48] Lauber P., Günter S., Könies A. and Pinches S.D. 2007 *J. Comput. Phys.* **226** 447
[49] Varela J. *et al* 2018 *Nucl. Fusion* **58** 076017
[50] Valovic M. *et al* 2000 *Nucl. Fusion* **40** 1569
[51] Wong K.L. *et al* 2000 *Phys. Rev. Lett.* **85** 996